



LJMU Research Online

Pan, Y, Simpson, CM, Kravtsov, A, Gómez, FA, Grand, RJJ, Marinacci, F, Pakmor, R, Manwadkar, V and Esmerian, CJ

Colour and infall time distributions of satellite galaxies in simulated Milky-Way analogues

<http://researchonline.ljmu.ac.uk/id/eprint/19369/>

Article

Citation (please note it is advisable to refer to the publisher's version if you intend to cite from this work)

Pan, Y, Simpson, CM, Kravtsov, A, Gómez, FA, Grand, RJJ, Marinacci, F, Pakmor, R, Manwadkar, V and Esmerian, CJ (2022) Colour and infall time distributions of satellite galaxies in simulated Milky-Way analogues. *Monthly Notices of the Royal Astronomical Society*. 519 (3). pp. 4499-4513.









LJMU has developed [LJMU Research Online](http://researchonline.ljmu.ac.uk/) for users to access the research output of the University more effectively. Copyright © and Moral Rights for the papers on this site are retained by the individual authors and/or other copyright owners. Users may download and/or print one copy of any article(s) in LJMU Research Online to facilitate their private study or for non-commercial research. You may not engage in further distribution of the material or use it for any profit-making activities or any commercial gain.

The version presented here may differ from the published version or from the version of the record. Please see the repository URL above for details on accessing the published version and note that access may require a subscription.

For more information please contact researchonline@ljmu.ac.uk

<http://researchonline.ljmu.ac.uk/>

Colour and infall time distributions of satellite galaxies in simulated Milky-Way analogues

Yue Pan ¹★, Christine M. Simpson ^{1,2,†}, Andrey Kravtsov ^{1,2,3}, Facundo A. Gómez ^{4,5},
Robert J. J. Grand ^{6,7}, Federico Marinacci ⁸, Rüdiger Pakmor ⁹, Viraj Manwadkar ¹
and Clarke J. Esmerian¹

¹Department of Astronomy and Astrophysics, The University of Chicago, Chicago, IL 60637, USA

²Enrico Fermi Institute, The University of Chicago, Chicago, IL 60637, USA

³Kavli Institute for Cosmological Physics, The University of Chicago, Chicago, IL 60637, USA

⁴Instituto de Investigación Multidisciplinar en Ciencia y Tecnología, Universidad de La Serena, Raúl Bitrán 1305, La Serena, Chile

⁵Departamento de Astronomía, Universidad de La Serena, Av. Juan Cisternas 1200 Norte, La Serena, Chile

⁶Instituto de Astrofísica de Canarias, Calle Vía Láctea s/n, E-38205 La Laguna, Tenerife, Spain

⁷Departamento de Astrofísica, Universidad de La Laguna, Av. del Astrofísico Francisco Sánchez s/n, E-38206 La Laguna, Tenerife, Spain

⁸Department of Physics and Astronomy ‘Augusto Righi’, University of Bologna, via Gobetti 93/2, I-40129 Bologna, Italy

⁹Max-Planck-Institut für Astrophysik, Karl-Schwarzschild-Str. 1, D-85748 Garching, Germany

Accepted 2022 December 8. Received 2022 December 8; in original form 2022 August 27

ABSTRACT

We use the Auriga simulations to probe different satellite quenching mechanisms operating at different mass scales ($10^5 M_\odot \lesssim M_* \lesssim 10^{11} M_\odot$) in Milky Way-like hosts. Our goal is to understand the origin of the satellite colour distribution and star-forming properties in both observations and simulations. We find that the satellite populations in the Auriga simulations, which was originally designed to model Milky Way-like host galaxies, resemble the populations in the Exploration of Local Volume Satellites (ELVES) Survey and the Satellites Around Galactic Analogs (SAGA) survey in their luminosity function in the luminosity range $-12 \lesssim M_V \lesssim -15$ and resemble ELVES in their quenched fraction and colour–magnitude distribution in the luminosity range $-12 \lesssim M_g \lesssim -15$. We find that satellites transition from blue colours to red colours at the luminosity range $-15 \lesssim M_g \lesssim -12$ in both the simulations and observations and we show that this shift is driven by environmental effects in the simulations. We demonstrate also that the colour distribution in both simulations and observations can be decomposed into two statistically distinct populations based on their morphological type or star-forming status that are statistically distinct. In the simulations, these two populations also have statistically distinct infall time distributions. The comparison presented here seems to indicate that this tension is resolved by the improved target selection of ELVES, but there are still tensions in understanding the colours of faint galaxies, of which ELVES appears to have a significant population of faint blue satellites not recovered in Auriga.

Key words: galaxies: dwarf – galaxies: evolution – galaxies: groups: general – galaxies: interactions – galaxies: star formation.

1 INTRODUCTION

One of the most fundamental properties of galaxies is their bimodal colour distribution. Galaxies generally fall into two types: a red sequence characterized by a lack of star formation, primarily composed of massive, quenched elliptical galaxies, and a blue cloud characterized by ongoing star formation, mainly composed of star-forming disc galaxies (Strateva et al. 2001; Baldry et al. 2004; Bell et al. 2004; Menci et al. 2005). Recent studies in the Local Volume (LV) have reproduced this colour bimodality in satellite galaxies (Carlsten et al. 2022). Understanding the underlying physical mechanisms that

cause this colour bimodality in dwarf galaxies is fundamental to our understanding of galaxy formation and evolution, because star-formation (SF) activity correlates with colour and, according to the hierarchical structure formation theory, all galaxies have once been dwarf galaxies (White & Frenk 1991).

However, there is ongoing debate about quenching processes in dwarf galaxies and in particular of dwarf satellites orbiting larger galaxies (see e.g. Sales, Wetzel & Fattahi 2022, for a recent overview). Studies in the Milky Way (MW) have found that except for a few massive objects (Lewis et al. 2007; Fraternali et al. 2009; Makarov et al. 2012; Karachentsev et al. 2015), all satellites of the MW within its virial radius are quenched. Extending to the Local Group (LG), nearly all dwarf galaxies with $M_* < 10^8 M_\odot$ that are satellites within 300 kpc of the MW or M31 have quiescent SF and little-to-no cold gas, but nearly all isolated dwarf galaxies (i.e. in the field) are star-forming and gas-rich (Mateo 1998; Grcevich & Putman

* E-mail: explorerpan@uchicago.edu

† Present address: ALCF, Argonne National Laboratory, Lemont, IL 60439, USA.

2009; Geha et al. 2012; Spekkens et al. 2014; Wetzel, Tollerud & Weisz 2015; Putman et al. 2021). This field-satellite dichotomy has been a strong indicator of environmental quenching (Lin & Faber 1983; McConnachie 2012; Slater & Bell 2014; Weisz et al. 2015; Wetzel et al. 2015): satellites are quenched by external processes once they enter the gravitational bounds of their massive hosts.

Moving beyond the LG, in the Local Volume (LV, ≤ 10 Mpc), Carlsten et al. (2022) found that the majority of low-mass satellites ($M_* \lesssim 10^7 M_\odot$) are quenched. However, the Satellites Around Galactic Analogs (SAGA) survey (Geha et al. 2017; Mao et al. 2021) found that most of the satellites within the virial radii of MW-like hosts in the same satellite mass range are actively star-forming, in stark contrast to LG and LV satellites (Karunakaran et al. 2021). The question of why there is such a big difference between satellites and isolated field dwarfs becomes urgent. Font et al. (2022) argued that by considering the differences in host mass distributions and observation selection effects, the huge discrepancy between the quenched fractions of low mass satellite galaxies in LG and isolated MW-like systems is significantly reduced.

Thanks to efforts in the theoretical front, we can now simulate MW and isolated environments for satellite galaxies at unprecedented resolution to understand the different physical mechanisms that drive galaxy quenching. Various processes have been proposed to stop star formation in satellite galaxies. Reionization is proposed to be driving quenching in low-mass dwarf galaxies (Dekel & Silk 1986; Thoul & Weinberg 1996; Gnedin 2000; Mayer et al. 2001; Brown et al. 2014; Weisz et al. 2014; Fillingham et al. 2016; Tollerud & Peek 2018; Rodriguez Wimberly et al. 2019). Galaxy interaction can also quench some satellite galaxies (Pearson et al. 2016, 2018). Internal processes such as stellar winds and supernova feedback can remove some part of the gas, but it is said to be insufficient for completely quenching the satellite (Agertz et al. 2013; Emerick et al. 2016).

External environmental processes such as ram pressure stripping – a process by which the cold gas of the satellites gets stripped when passing through the circumgalactic medium (CGM) of the host – are said to be the dominant quenching mechanism for satellite masses $10^5 M_\odot \lesssim M_* \lesssim 10^8 M_\odot$ (Gunn & Gott 1972; Murakami & Babul 1999; Tonnesen & Bryan 2009; Bahé & McCarthy 2015; Fillingham et al. 2016; Kazantzidis et al. 2017; Simpson et al. 2018; Digby et al. 2019; Fillingham et al. 2019). Ram pressure is consistent with the rapid quenching time-scale ($1 \sim 2$ Gyr) of these satellite galaxies upon infall (Fillingham et al. 2015). Tidal stripping can also boost the efficiency of ram pressure stripping by diminishing the overall gravitational potential of the satellite galaxy (Mayer et al. 2006). Because more massive satellites are better able to retain their gas reservoirs (Simpson et al. 2018; Garrison-Kimmel et al. 2019) compared to lower mass satellites when interacting with hosts of the same mass, environmental quenching is less efficient for more massive satellite galaxies.

Starvation or strangulation – a scenario in which gas accretion onto the satellite galaxy is stopped after infall – can quench more massive satellite galaxies ($M_* \sim 10^8$ – $10^{11} M_\odot$) (van den Bosch et al. 2008; McGee, Bower & Balogh 2014; Wheeler et al. 2014; Fillingham et al. 2015; Phillips et al. 2015; Davies et al. 2016; Trussler et al. 2020) and the time-scale of starvation is comparable to the gas depletion time-scale (Huang et al. 2012; Wetzel et al. 2013; Wheeler et al. 2014; Fillingham et al. 2015). For environmental processes, Garrison-Kimmel et al. (2019) used the FIRE simulations to identify differences in histories between ‘satellite versus central’ galaxies and in different environments ‘LG versus individual MW versus isolated dwarf central’. They found that around individual MW-mass

hosts, central galaxies in the ‘near field’ have more extended SFH than their satellite counterparts: the former more closely resemble isolated (true field) dwarfs, but this difference is muted in LG-like environments, suggesting that the paired halo nature of LG may regulate star formation in dwarf galaxies even beyond the virial radii of the MW and M31. Moreover, Hausammann, Revaz & Jablonka (2019) used a wind tunnel and a moving box technique to simulate both the ram pressure and tidal forces, and they found that while ram pressure is very efficient at stripping the hot and diffuse gas of the dwarf galaxies, it can remove their cold gas ($T < 10^3$ K) only in very specific conditions.

In this paper, we use the Auriga project (Grand et al. 2017), a suite of 30 cosmological magnetohydrodynamical zoom simulations of galaxy formation in Milky Way mass haloes, to probe further into the quenching mechanisms of satellite galaxies. We start by comparing the Auriga simulations with observations in terms of luminosity function, quenched fraction, and colour–magnitude diagram to establish how the results from simulations compare with observations. We then draw a connection between the colour and infall time distributions in the simulations by exploring time-scales associated with satellite evolution as measured in the simulations. Finally, we identify different quenching mechanisms operating on different mass scales.

The structure of this paper is as follows. In Section 2, we describe the Auriga simulations and the methods we used to obtain satellite NUV- g colours in the Auriga simulations. In Section 3, we compare the Auriga simulations to the ELVES sample in terms of luminosity function, quenched fraction, and colour–magnitude diagram. In Section 4, we use the Auriga simulations to determine different time-scales associated with quenching and explore the possible connection between quenching time-scales and the simulated mass, colour, and magnitude of satellites. In Section 5, we discuss the comparison between the Auriga simulations and observations from SAGA and ELVES, and with other simulations with different implementations of underlying physics. Finally, we present our conclusions in Section 6.

2 METHODS

In this section, we introduce the Auriga simulations and the methods we used to obtain NUV- g colours for satellites in the Auriga simulations.

2.1 The Auriga simulations

In this study, we use the Auriga simulations (Grand et al. 2017) – a suite of cosmological zoom-in simulations of $\approx 10^{12} M_\odot$ haloes designed to simulate the formation of MW-sized galaxies. The Auriga simulations were run with the N -body+magnetohydrodynamics code AREPO (Springel 2010; Pakmor et al. 2016) and include many of the physical effects important in galaxy formation, including gravity, gas cooling, magnetic fields, star-formation, energetic feedback from stars and black holes, and metal enrichment (Grand et al. 2017).

We focus most of our study on the original 30 haloes of the Auriga suite that have a baryon mass resolution of $\sim 5 \times 10^4 M_\odot$ and a minimum physical gravitational softening length of 369 pc after $z = 1$ (that scales with the scale factor prior to $z = 1$). We also consider resimulations of six haloes with eight times better mass resolution that have a baryon mass resolution of $\sim 6.7 \times 10^3 M_\odot$ and a minimum softening length of 185 pc. Following the conventions of the Auriga project, we call the lower resolution simulations ‘Level

4' simulations and the higher resolution simulations 'Level 3.' It has been demonstrated that the properties of galaxies we focus on in this study are well converged at the Level 4 resolution with the Auriga model for interstellar medium, star formation, and feedback (Grand et al. 2021).

We make use of the Auriga halo catalogues created during the simulations that identify dark matter haloes with a friends-of-friends algorithm (Davis et al. 1985) and gravitationally bound subhaloes identified with the SUBFIND code (Springel et al. 2001). We track inheritance between subhaloes with the merger tree code LHALOTREE (Springel et al. 2005; De Lucia & Blaizot 2007). In Level 4, we have a total of 128 snapshots, and the maximum spacing between snapshots is 167 Myr which decreases towards higher redshift. In Level 3, we have a total of 64 snapshots, and the maximum spacing between snapshots is 372 Myr which also decreases towards higher redshift.

2.2 NUV-g colours of Auriga satellites

The absolute magnitudes in the U , B , V , R , g , r , i , and z bands computed using models of Bruzual & Charlot (2003) are provided for each halo and subhalo in the Auriga catalogues (Grand et al. 2017). To facilitate comparison of the colour distribution with observations of Carlsten et al. (2022), we also computed *GALEX* near-UV (NUV) magnitudes for each satellite using the Flexible Stellar Population Synthesis (FSPS) code (Conroy, Gunn & White 2009; Conroy & Gunn 2010)¹ with its Python bindings PYFSPS.² Specifically, for each surviving satellite at $z = 0$, we treated the satellite's stellar particles (with known metallicity, age, and mass) as a single-age stellar population and combined their individual luminosity to get total satellite luminosity.

We use the default MIST isochrones (Choi et al. 2016; Dotter 2016), Chabrier IMF (Chabrier 2003), and MILES spectral library (Vazdekis et al. 2010; Falcón-Barroso et al. 2011) in FSPS, where the solar metallicity is 0.0142. However, creating a different SSP for each star particle is computationally expensive, since we have $\sim 5 \times 10^7$ particles in all the satellites. Instead, we use a method similar to that used by the Auriga SUBFIND code to compute the luminosity for each star particle by taking the a 2D grid of metallicity and age, apply the grid to FSPS `get_mags` function to compute the SDSS g -band and *GALEX*-NUV band magnitudes for each grid value, then interpolate all the star particles magnitudes based on this magnitude grid. We use the same age–metallicity grid used by Auriga's SUBFIND code. We then convert the magnitudes into luminosity, add up all the particle luminosities in one satellite, and finally convert back to magnitudes and add an offset related to the particle mass to calculate the absolute satellite magnitude.

As an additional check, we computed the difference between the satellite absolute g -band magnitude we calculated and the satellite absolute g -band magnitude tabulated in the Auriga catalogue as a function of the satellite g -band magnitude in the catalogue. We apply two different 3D radial cuts: $r < 300$ kpc and $r < 150$ kpc. We compute the 3D distance between the satellite and the host and apply a constant radial cut (300 kpc or 150 kpc) at all look-back times to select satellites. No matter what the radial cut is, the discrepancy between our value and the catalogue value is less than 0.1 mag, indicating that our NUV and g -band magnitude calculation is robust and consistent with the catalogue values.

3 OBSERVABLE PROPERTIES OF SIMULATED SATELLITES

In this section, we present the luminosity function, the colour distributions, and the colour–magnitude diagram for satellites in the Auriga simulations. We also compare these trends the ELVES and SAGA observational surveys.

3.1 Luminosity function

We first compare the differential and cumulative luminosity functions (LFs) of satellites in the Auriga simulation and ELVES and SAGA sample within radial cuts of $r_{\text{proj}} < 300$ kpc and $r_{\text{proj}} < 150$ kpc. Note that the radial cut in the Auriga simulations is 3D, whereas the radial cut in ELVES and SAGA samples is a 2D line-of-sight projection. There are 21 ELVES galaxies surveyed out to 300 kpc, and 30 hosts surveyed out to 150 kpc. 33 hosts are surveyed out to 300 kpc in SAGA. We apply the same radial cuts to the 30 hosts in the Auriga Level 4 haloes, and compare the differential and cumulative V -band LF of the simulated satellites with the LF of ELVES and SAGA satellites. Note that the high-resolution zoom region around each Auriga host extends to ~ 1 Mpc, well beyond the radial extent of the ELVES and SAGA satellite sample.

The comparison is shown in Fig. 1. The two vertical dashed lines in Fig. 1 mark the magnitude range of $-15 < M_V < -12$. Carlsten et al. (2022) found that satellites in the ELVES sample transition in this magnitude range from being mostly late type to mostly early type. We thus also focus on satellites in this magnitude range for comparison with observations and to understand the mechanisms that drive this shift in properties. We define star-forming satellites in the simulations as having a star formation rate $\text{SFR} > 0$ at $z = 0$. Late-type ELVES satellites (which are more likely to be star forming) are defined by visually inspection of their morphology (see Section 6.2 of Carlsten et al. 2022, for a detailed discussion). In SAGA, quenched satellites are defined as having $\text{EW}(\text{H}\alpha) < 2 \text{ \AA}$.

We count the number of satellites in each magnitude bin for each sample we explore. Following Carlsten et al. (2022), we quantify the variation in the luminosity function between hosts by computing the standard deviation of satellite abundance across different hosts in both Auriga, SAGA and ELVES and dividing it by $\sqrt{N_{\text{host}}}$. Thus, the error bars shown in Fig. 1 denote the intrinsic host-to-host scatter in satellite abundance.

The top panel in Fig. 1 shows that there are somewhat more satellites per host per magnitude bin in the Auriga simulations than in the ELVES and SAGA sample on the bright end of LF, but both are consistent within the errorbars. This trend is reversed as we proceed to fainter satellites. The middle and bottom panels showing differential LFs indicate that this trend is a combination of different trends for the star-forming and quenched galaxies. LFs of star-forming galaxies in the simulation are quite close to observed ones, especially in the luminosity range $-15 < M_V < -12$. The LF shapes are somewhat different, however. The shapes of LFs of quenched/early-type galaxies, on the other hand, are quite similar but the amplitude of the simulated LFs is ~ 1.3 – 2 times lower than in the ELVES sample. We found that this lack of satellites in Auriga below $M_V = -12$ is not due to resolution limits by confirming the convergence of L3 and L4 LF down to $M_V \sim -8$. We also note that Grand et al. (2021) shows convergence of the model for a single host halo down to $M_V \sim -8$ with resolution greater than L3. Notably, the transition from the mostly quenched to mostly star-forming satellites in both the Auriga simulations and ELVES and SAGA sample occurs in the range $-15 < M_V < -12$.

¹<https://github.com/cconroy20/fpsps>

²<https://github.com/dfm/python-fpsps>

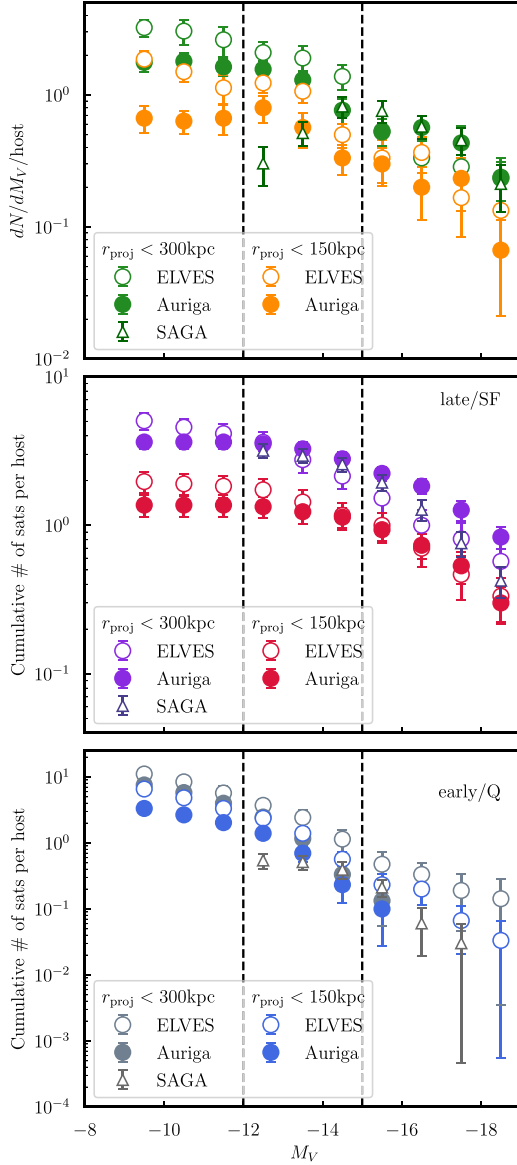


Figure 1. The satellite luminosity function (LF) in the Auriga simulations and SAGA and ELVES sample. We only include SAGA satellites brighter than $M_V = -11.9$ since this is the magnitude limit cut. Top: Differential luminosity functions for observed satellite galaxies in ELVES (open circles), SAGA (open dark green triangles), and simulated satellites in Auriga (solid green circles) are shown. The green (orange) points show LF of satellites within 300 kpc (150 kpc) of the host centre. In Auriga this is a 3D radial cut, whereas in ELVES this is a line-of-sight 2D projection radial cut. Middle: Cumulative LFs for late-type satellite galaxies in the ELVES sample and star-forming satellite galaxies in and SAGA and Auriga within 150 and 300 kpc from the galaxy centre shown by violet, dark blue, and red points, respectively. Bottom: Cumulative LFs for early-type satellite galaxies in the ELVES sample and quenched satellite galaxies in SAGA and Auriga within 150 and 300 kpc shown by grey, dark grey, and blue points, respectively. Overall, the shape of LFs in both simulation and observation is similar for all three cases, but ELVES tends to have more faint satellites than Auriga. Within the magnitude cut of $-15 \lesssim M_V \lesssim -12$ shown as the vertical dashed lines, the Auriga LF is in reasonable agreement with that in the ELVES sample for both late- and early-type galaxies. Auriga does not have bright quenched satellites within the radial cut of 150 kpc. The SAGA differential LF drops around $M_V \sim -12$ compared to both ELVES and Auriga, primarily due to a drop of quenched satellites shown in the bottom panel. The errorbars show the error in the mean number of satellites per host within each magnitude bin.

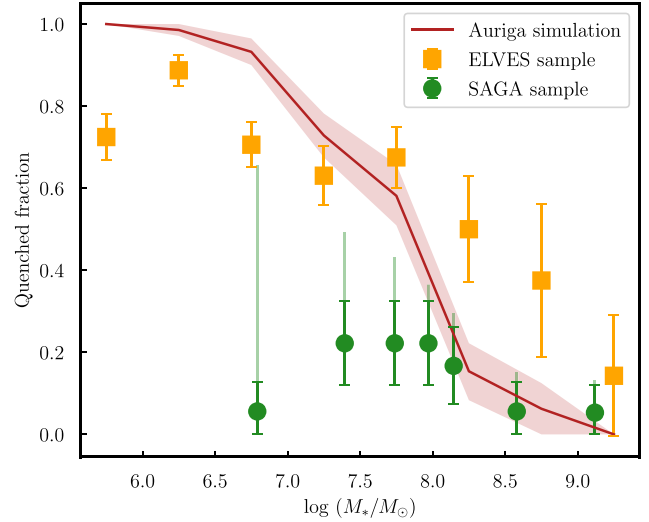


Figure 2. Quenched fraction as a function of log stellar mass for ELVES, SAGA surveys and the Auriga simulations. Quenched fraction within each mass bin is defined as the number of quenched satellites divided by the total number of satellites in this mass bin. In the SAGA survey, a satellite galaxy is defined as quenched if it has no $H\alpha$ emission, while in the ELVES survey, it is defined by visually classifying it as early-type. In the Auriga simulations, it is defined as its gas phase SFR = 0 at the end of the simulation. We apply the redshift incompleteness in Mao et al. (2021) to the SAGA quenched fraction and plot them as light green bars. We plot the error in the mean quenched fraction within each mass bin as errorbars (SAGA, ELVES) and a red-shaded region (Auriga).

3.2 Quenched fraction

In Fig. 2 we compare the satellite quenched fraction as a function of the logarithm of stellar mass in the ELVES and SAGA surveys to the Auriga simulations. We apply a 3D radial cut of 300 kpc for the Auriga sample and a 2D line-of-sight radial cut of 300 kpc for the ELVES and SAGA sample. In the Auriga simulations, we define a satellite as quenched if its gas phase SFR = $0 \text{ M}_\odot \text{ yr}^{-1}$ at the end of the simulation. Karunakaran et al. (2021) investigated other definitions of SFR such as the average mass of star particles formed over the last gigayear and found that both estimates of SFR produce similar results in terms of the quenching status of satellite galaxies. Moreover, by analysing the left-hand panel of fig. 2 in Karunakaran et al. (2021), the specific SFR (sSFR) values for most star-forming satellite galaxies (SFR > $0 \text{ M}_\odot \text{ yr}^{-1}$) are above 0.01. Therefore, a threshold of sSFR = 0.01 to distinguish quenched and star-forming satellite galaxies would produce similar results in our analysis. In the ELVES survey, we use morphology-based classification of quenched satellites of Carlsen et al. (2022), while SAGA satellites are classified using $H\alpha$ emission by Mao et al. (2021). All the errorbars are estimated using a bootstrap sampling strategy.

Fig. 2 shows that although the quenched fraction in the SAGA survey is significantly smaller than that in the Auriga simulation for satellites with $M_* \lesssim 10^8 \text{ M}_\odot$, the new ELVES survey has a much higher quenched fraction for such satellites and is much closer to the quenched fraction measured in the Auriga simulations. For satellites with $M_* \gtrsim 10^8 \text{ M}_\odot$, the quenched fraction in simulations matches that in the SAGA survey and is smaller than the fraction in the ELVES survey, but consistent at the 2-sigma level. On the lower mass end, the Auriga simulations is inconsistent with both ELVES and SAGA but the discrepancy with ELVES is less pronounced. A more recent study

by Karunakaran et al. (2022) shows that the discrepancy between SAGA and ELVES could potentially be significantly reduced by using a consistently derived sSFR and absolute magnitude limit in both samples.

3.3 Colour–magnitude diagram

Fig. 3 shows the NUV- g colour as a function of the g -band absolute magnitude M_g for satellites in the ELVES and Auriga Level 3 and Level 4 simulations. It shows that ELVES and Auriga satellites basically occupy the same region in the NUV- g and M_g parameter space in the magnitude range $-15 < M_g < -12$, but the simulated satellite population is deficient in blue, faint satellites in the lower left of this parameter space that are present in ELVES. We discuss in detail the possible reasons for this in Section 5.1.

This figure shows that there is a transition from early-type or quenched satellites to late-type or star-forming within the magnitude range $-15 < M_g < -12$, for both Auriga and ELVES satellites. Satellites that are brighter than $M_g \sim -15$ are primarily star-forming or late-type in both Auriga and ELVES.

We also include Auriga Level 3 satellites in the colour magnitude diagram. Due to eight times better resolution compared to Level 4, satellites in the Level 3 simulation reach much fainter satellites ($M_g \gtrsim -8$). Nevertheless, the improvement in resolution does not remedy the discrepancy between the simulations and observations caused by dearth of blue, faint satellites in the former.

To examine this transition further, Fig. 4 shows the distribution of NUV- g colour in the ELVES and Auriga L4 satellites. We separate ELVES satellites into late- (blue shaded histogram) and early-types (red-shaded histograms), and Auriga satellites into quenched (red-shaded histograms) and star-forming (blue shaded histogram). The p -value for the red and blue histograms to be drawn from the same parent distribution for both ELVES and Auriga satellites is $< 10^{-5}$, indicating a statistically significant difference. Thus, for both observation and simulations, we find two distinct populations with respect to satellite colour.

Overall, results presented here show that the Auriga simulations capture certain qualitative trends such as luminosity function, quenched fraction, and the two distinct populations in terms of NUV- g colour that are also found in observed samples in ELVES and SAGA. We now turn to exploring the physical processes that drive satellite quenching in the simulations. We will return to discussing the comparisons between simulations and observations and what that means for the Auriga model in Section 5.

4 PHYSICAL EVOLUTION TIME-SCALES AND STAR FORMATION QUENCHING

Given that luminosity function, quenched fraction, and the two distinct populations in terms of NUV- g colour in the Auriga simulations matches the distribution of observed galaxies in the ELVES sample reasonably well, we can use simulations to gain insight into the quenching processes that separate these two types of satellites. To this end, we consider five different characteristic epochs and time-scales associated with evolution of satellites in simulations:

(i) The quenching time τ_{90} is defined as the look-back time when 90 per cent of the satellite stars have formed,³

³Weisz et al. (2015) found that using τ_{90} instead of τ_{100} could potentially minimize the uncertainty induced by modelling blue straggler populations. For star-forming satellite galaxies, this quantity does not indicate their

(ii) The gas loss time, $t_{\text{gas loss}}$, is defined as the look-back time when the gas mass fraction (the ratio of the gas mass to total mass) first drops below 0.01.

(iii) The infall time, t_{infall} , is the look-back time when the satellite first crosses the virial radius r_{200} .

(iv) The time interval between t_{infall} and τ_{90} , $t_{\text{delay}} = t_{\text{infall}} - \tau_{90}$, which gauges whether quenching occurs before or after satellite infall. A positive t_{delay} means the system stopped forming stars after infall and a negative value means it stopped before infall.

(v) The look-back time when the ram pressure experienced by gas in the satellite reaches a local maximum after infall and is closest to $t_{\text{gas loss}}$, t_{rmax} . We only compute this time-scale for satellites quenched after infall to make sure we are only including satellites for which environmental processes are relevant. We require the local ram pressure maximum to be closest to $t_{\text{gas loss}}$ to make sure that we are finding the most relevant pericentre passage that quenches the satellite.

To calculate the ram pressure, we use the scaling of the ram pressure force with background gas density, ρ_{CGM} , and relative satellite velocity, v_{sat} , that follows from dimensional considerations:

$$P_{\text{ram}} = \rho_{\text{CGM}} v_{\text{sat}}^2. \quad (1)$$

We estimate ρ_{CGM} using spherically averaged density profile extending out to $4r_{200}$ around each host in each time snapshot, interpolating the density profiles at the subhalo's position to get ρ_{CGM} at a specific epoch between snapshots (see Simpson et al. 2018, for a detailed discussion of this approach to computing P_{ram}). This calculation of ρ_{CGM} may be biased in two ways. First, in some cases, the host halo density profile is not homogeneous. Secondly, there is a certain error in estimating the pericentric passage time due to finite spacing between simulation snapshots. This can potentially be improved using orbit integration method to interpolate between snapshots (Richings et al. 2020), but we postpone exploration of such methods to future work.

As an illustration of how different time-scales relate to satellite observables, Fig. 5 shows evolution of ram pressure, distance to the host, star formation, and gas fraction for three satellites of different M_g and stellar mass. The faintest satellite is quenched before infall and its star formation is halted at an early times (~ 6 Gyr). The intermediate luminosity satellite is quenched after infall, likely by environmental effects such as ram pressure stripping. The local ram pressure peak that we identify as being the most relevant in quenching this satellite is marked as a purple star. Although the second later ram pressure peak has a larger amplitude, it is the first peak that strips all of the gas as can be seen in the gas fraction panel. There is no gas left at the time of this second ram pressure peak. The luminous satellite is still forming stars at $z = 0$. Although it experienced two local ram pressure peaks after infall, it is massive enough to resist these ram pressure events.

4.1 Satellite infall time distribution

Simpson et al. (2018) found indications that satellite infall times in the Auriga simulations are bimodal (see their fig. 11). Here, we re-investigate the infall time distribution using the optimal histogram bin width estimated with the objective Bayesian method of Knuth (2006) for each sample we consider in Fig. 6.

quenching status; rather, it is an upper bound of the look-back quenching time.

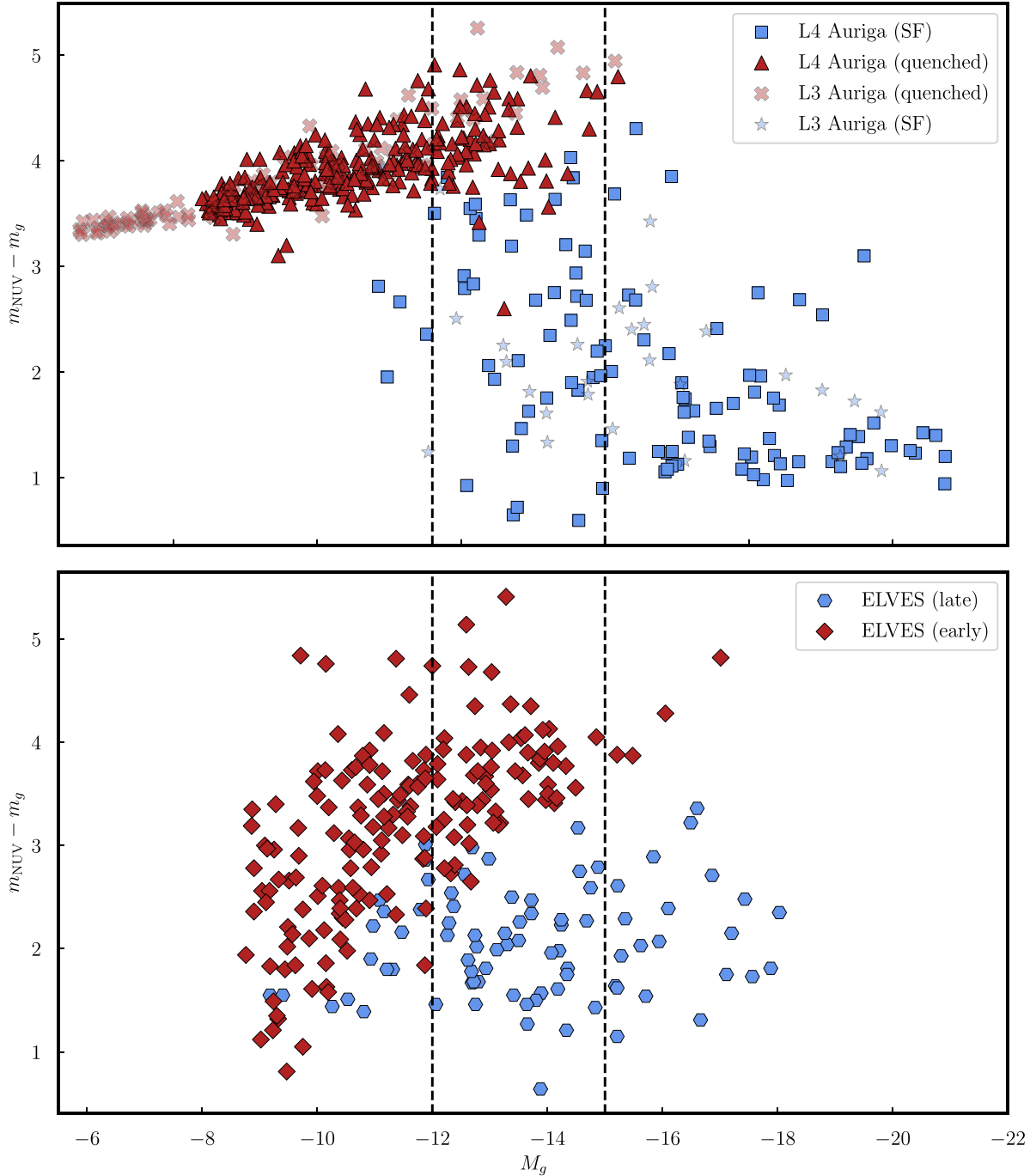


Figure 3. The colour–magnitude diagram for satellites in the ELVES sample and Auriga simulation selected within 300 kpc of the host centres. The top (bottom) panel shows the CMD for Auriga (ELVES) satellites. The Auriga satellites are separated into quenched (red triangles) and star-forming (blue squares), while the ELVES satellites are separated into early-type (red open diamonds) and late-type (blue open hexagons). The two vertical dashed lines are the magnitude cut $-15 \lesssim M_g \lesssim -12$. Overall the distribution of model galaxies is similar in the magnitude range $-15 < M_g < -12$. There are fewer blue, faint satellite galaxies in the Auriga sample compared to the ELVES sample. We also include satellites from the higher resolution Auriga Level 3 simulation, denoted as stars and crosses, which probe fainter ($M_g > -8$) regime.

We apply the Kolmogorov–Smirnov (KS) statistics to the infall time distributions of blue and red distributions in both panels to quantify the p -value that the two populations are drawn from the same parent distribution and find that it is less than 10^{-5} . This indicates that these distributions are statistically distinct and thus in agreement with conclusions of Simpson et al. (2018) that distributions of infall times of star-forming and quenched satellites are statistically different.

This, in turn, implies that environmental effects play an important role for at least a substantial fraction of satellites.

In Fig. 7, we combine Figs 4 and 6 to directly probe the relation between NUV- g colour and t_{infall} . There are two obvious groups of points: one in the upper left with early t_{infall} and red colour (NUV- $g \geq 3.5$), and the other in the lower right with late t_{infall} ($t_{\text{infall}} \leq 6$ Gyr) and blue colour (NUV- $g \leq 3$). This indicates that early infall

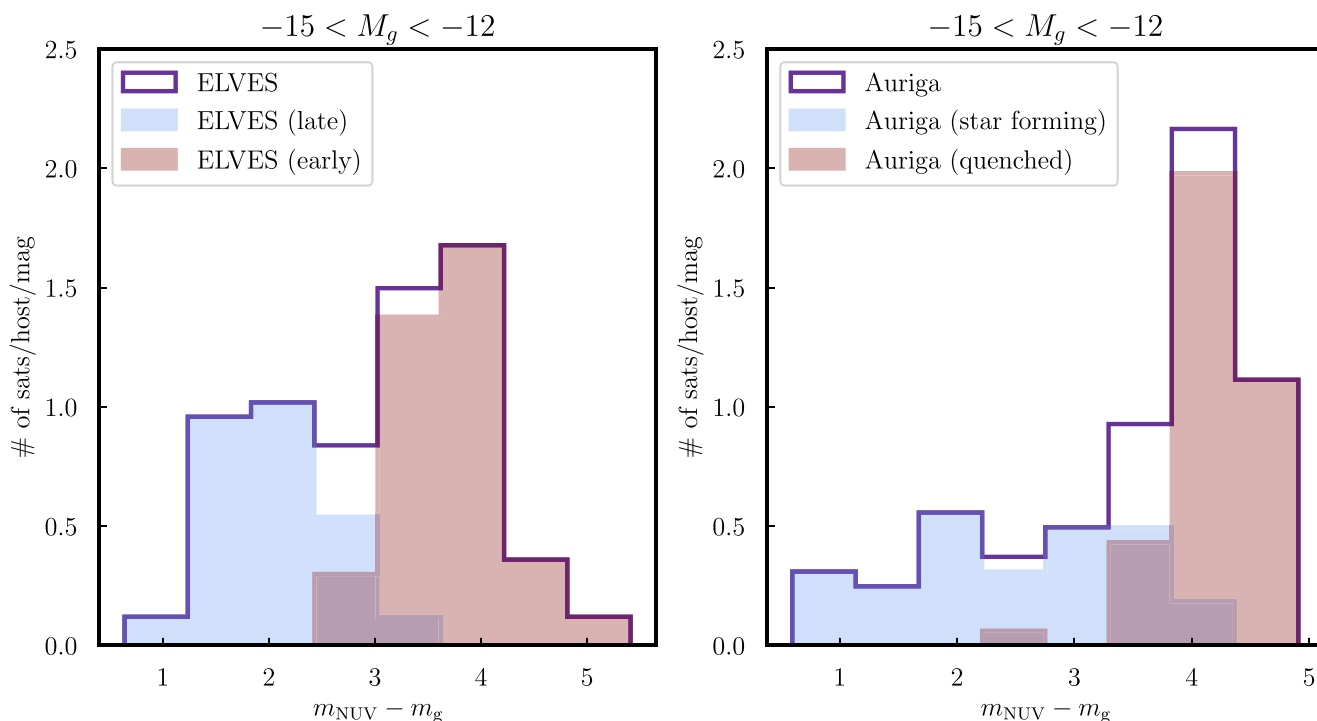


Figure 4. The distribution of NUV- g colours in the Auriga and ELVES samples in the magnitude range $-15 < M_g < -12$. Left-hand panel: The distribution of NUV- g colour of satellites in the ELVES sample (purple histogram) and for the early (red) and late type (blue) satellites. The p -value of the hypothesis that blue and red histograms are drawn from the same distribution is $< 10^{-5}$, indicating that the two populations are intrinsically different. Right-hand panel: The distribution of NUV- g colour for the Auriga satellites (purple histogram), and for star forming (blue) and quenched (red) satellites separately. The p -value in this case is also $< 10^{-5}$ and thus star forming and quenched satellites in the Auriga are similarly different to observed systems. The red peak in Auriga is somewhat redder, while the blue peak is broader and lower than for the ELVES satellites. The p -value for the ELVES and Auriga colour distributions is 8×10^{-4} , so we cannot rule out the possibility that they are different. Note that we do not show that the colour distribution is bimodal – we simply show that there are two distinct populations in the colour distribution.

satellites tend to be red and quenched, while late infall satellites are blue and star-forming. There are some recent infall satellites with red colour (upper right), but they have low stellar mass ($M_* \leq 10^7 M_\odot$), indicating that they are not able to retain their gas after interacting with their hosts and get quenched on short time-scales. Dwarfs that never fall within the virial radius of their host (black triangles) display a range of colour, but most of them have blue colours. Studies have shown that field dwarfs tend to be bluer than their satellite counterparts (Geha et al. 2012). Although we do not have a statistical sample of real dwarfs here, the population of satellites that never fall within the virial radius of their host does demonstrate a slight trend of bluer colour.

4.2 How t_{infall} relates to τ_{90}

The panels of Fig. 8 show distribution of satellite galaxies in three absolute magnitude ranges in the $t_{\text{infall}} - \tau_{90}$ plane. The upper panel of Fig. 8 shows that most faint satellites with $M_g > -12$ are quenched before they became satellites (i.e. have $\tau_{90} < t_{\text{infall}}$). There is a group of low-luminosity satellites in Level 3 (marked by open symbols in both Figs 8 and 9) that have a look-back τ_{90} in the range ≈ 10 – 12.5 Gyr ($z \approx 2$ – 6), after the end of the epoch of reionization in the Auriga simulation at $z = 6$ (Vogelsberger et al. 2013; Grand et al. 2017). We only have such low-mass systems in Level 3 simulations because these systems are not resolved in the Level 4 simulations. The quenching mechanism here is most likely suppression of gas accretion due to UV heating after reionization. Indeed, previous

studies found that reionization mainly affects satellites with a stellar mass $M_* \lesssim 10^6 M_\odot$ (e.g. Bose, Deason & Frenk 2018; Kravtsov & Manwadkar 2022).

The middle panel of Fig. 8 shows a sharp transition in the $t_{\text{infall}} - \tau_{90}$ plane: satellites in the magnitude range $-15 < M_g < -12$ are either still star forming or quenched by environmental processes since they have $t_{\text{infall}} > \tau_{90}$. The bottom panel of Fig. 8 shows that luminous satellites ($M_g < -15$) are predominantly star forming, and they became satellites less than ≈ 7 Gyr ago (i.e. after $z \sim 1$). Indeed, there are some massive satellites with $t_{\text{infall}} < 2$ Gyr in the lower left-hand region of the bottom panel that are actively star-forming, similar to Large and Small Magellanic Clouds. The lack of quenched massive satellites with early t_{infall} is likely due to their disruption or merging with the central galaxy.

Fig. 9 also shows that a substantial fraction of satellites with stellar masses in the range of $M_* \lesssim 10^7 M_\odot$ are quenched before infall (negative t_{delay}), although this fraction decreases with increasing M_* . This quenching is thus likely due to internal processes such as stellar feedback, which can drive out most of the gas and quench dwarf galaxy for an extended period of time (see e.g. Rey et al. 2022), or a combination of gas suppression due to UV heating and internal feedback (Rey et al. 2020), or interactions with the filaments of the cosmic web (Benítez-Llambay et al. 2013).

In contrast with small-mass galaxies with $M_* < 10^7 M_\odot$ that are predominantly quenched and red, there are both star-forming and quenched galaxies among more massive satellites with the fraction of star-forming galaxies increasing with stellar mass. Figs 8 and 9

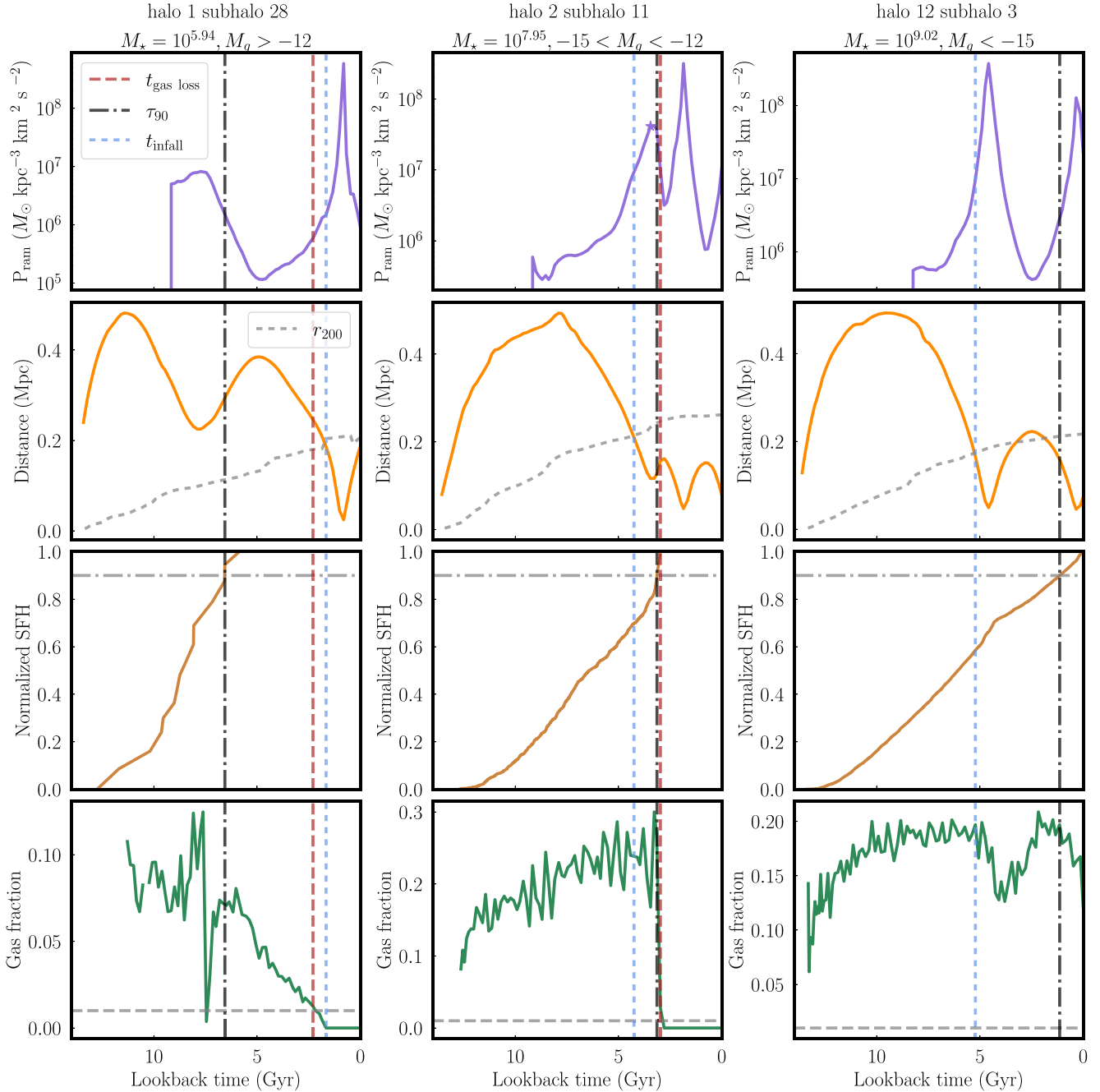


Figure 5. An illustration of ram pressure (top), distance from the centre of the host (second row from top), star formation history (SFH, third row from the top) and gas fraction (bottom) as a function of look-back time for three satellites in three different magnitude bins: $M_g > -12$, $-15 < M_g < -12$, $M_g < -15$. The dashed lines overplot three time-scales, $t_{\text{gas loss}}$, t_{infall} , τ_{90} as red, blue, and black dashed lines, respectively. The black dashed line in the distance row shows the evolution of the host r_{200} (the radius within which the halo’s mean density is 200 times greater than the critical density of the universe). A horizontal dot-dashed grey line in the normalized SFH and gas fraction rows show a SFH value of 0.9 and a gas fraction value of 0.01, respectively.

together show that quenched satellites with $M_* \gtrsim 10^7 M_\odot$ tend to have earlier infall times. The quenching of star formation in satellites of this mass range is thus predominantly due to environmental effects. Given that these effects operate on a certain time-scale, satellites that accrete sufficiently early are quenched, while those that accrete late can remain star forming (we will discuss this further in the next section).

Fig. 9 also shows that intermediate mass satellites $10^7 M_\odot \lesssim M_* \lesssim 10^8 M_\odot$ quench at the time close to the infall epoch. Note that crossing r_{200} (t_{infall}) marks the onset of environmental effects only very approximately because galaxies can start to experience enhanced tidal and ram pressure forces well before crossing the virial radius (e.g. Behroozi et al. 2014). Thus, small negative t_{delay} can still be due to quenching by environmental processes.

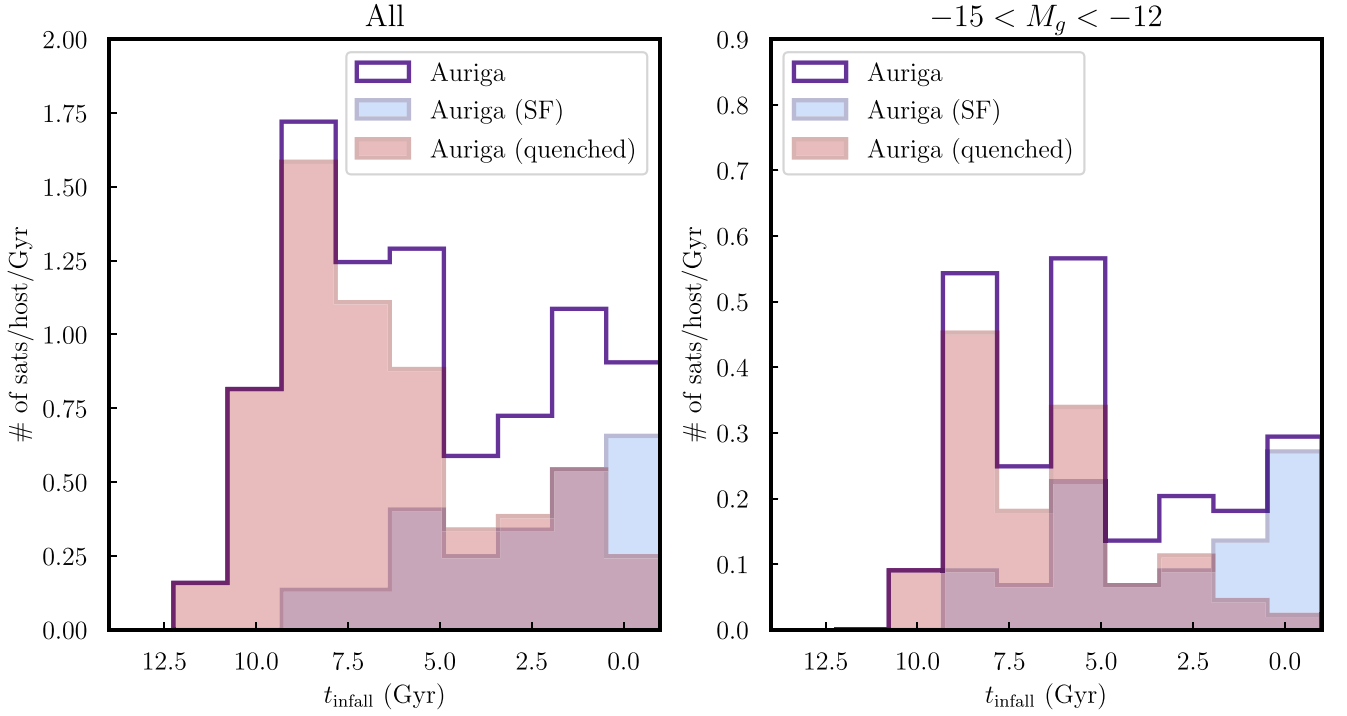


Figure 6. The distribution of look-back infall times in the Auriga simulations. Left-hand panel: Distribution of look-back infall times per host per Gyr for all satellites within 300 kpc of the galaxy at $z = 0$ (purple line) in the Auriga simulation and for the star-forming (blue) and quenched satellites (red). The p -value for the red and blue histograms to be drawn from the same distribution $< 10^{-5}$, indicating that the two populations are intrinsically different. Right-hand panel: The same distribution, but for all satellites within the magnitude cut $-15 \leq M_V \leq -12$ for a direct comparison with the ELVES data. The p -value in this case is 1.5×10^{-3} . Here again quenched satellites tend to have earlier infall times than star-forming ones, in agreement with fig. 2 in Fillingham et al. (2019).

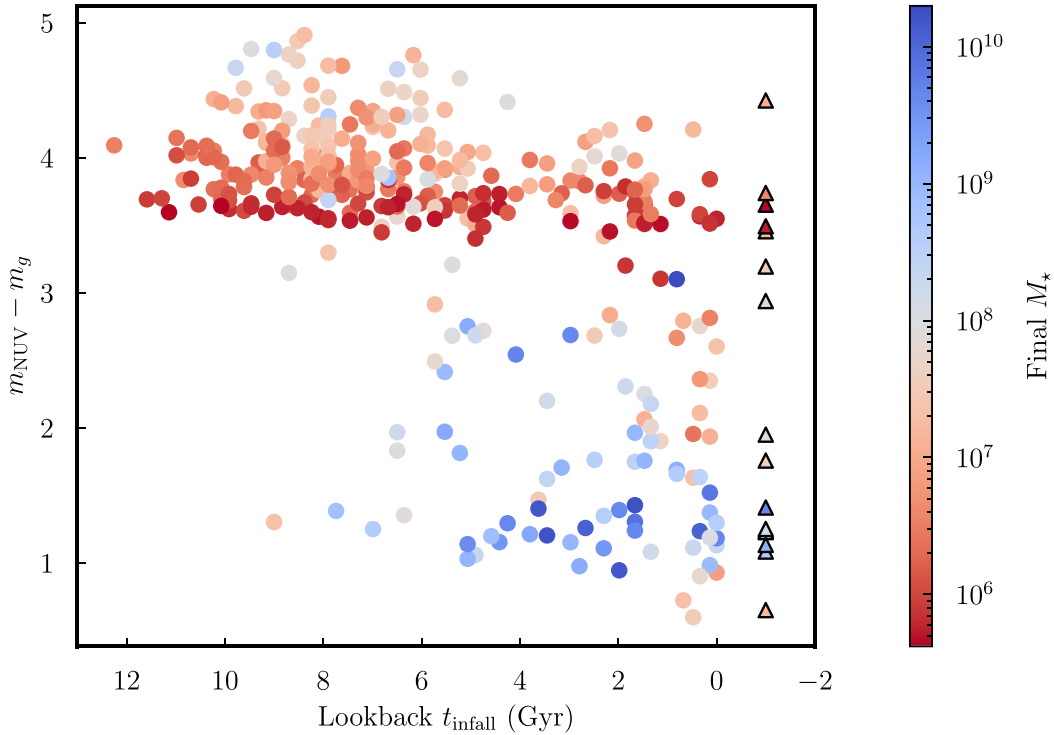


Figure 7. NUV- g colour versus t_{infall} colour coded by final M_* for all satellites in L4 that are within 300 kpc of their host by the end of the simulation. This panel connects the colour distribution with the infall time distribution. The triangles with a black frame represent satellites that are within 300 kpc of their host by the end of the simulation but outside of the virial radius, thus they are never environmentally influenced by their host. We denote their $t_{\text{infall}} = -1$ Gyr.

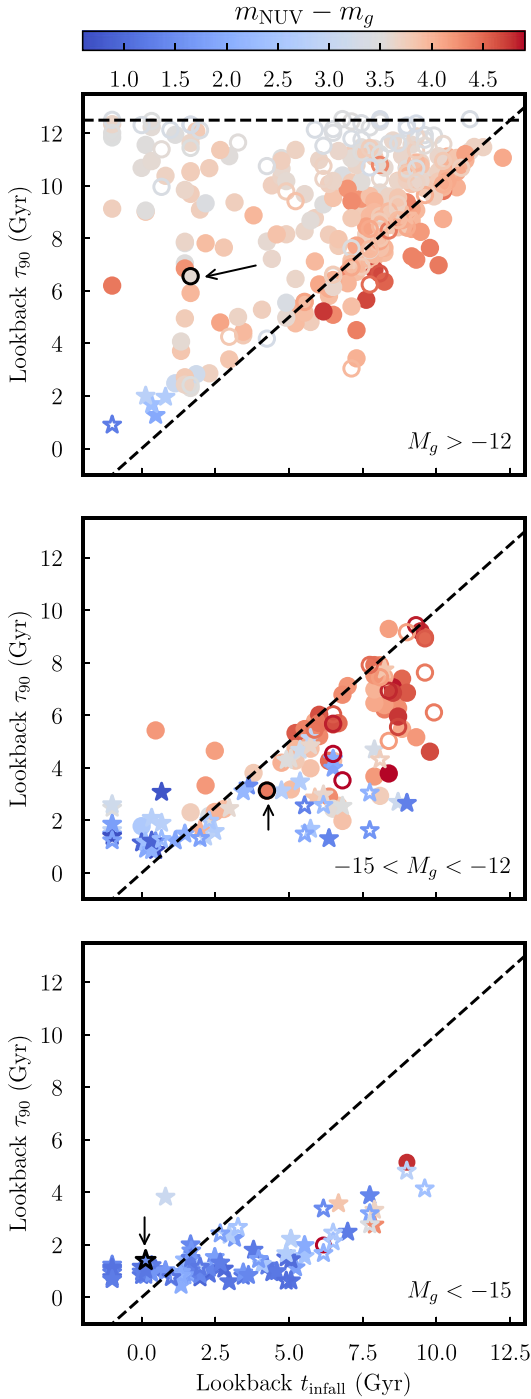


Figure 8. τ_{90} as a function of t_{infall} . Satellite points in all panels are colour-coded by their NUV- g colour shown in the colour bar. Different rows show satellites in three different magnitude bins. The open (solid) symbols refer to the satellites in Level 3 (Level 4) simulation. The star symbols refer to satellites that are star-forming, while circles refer to quenched satellites in our definition. The three examples in different magnitude bins in Fig. 5 are indicated by black arrows and a black frame. Satellites that never cross the host’s virial radius but are within 300 kpc by the end of the simulation are assigned the infall time of $t_{\text{infall}} = -1$. The diagonal dashed line delineates positive and negative t_{delay} : above this line, nearly all satellites are faint, low-mass, and quenched before infall, whereas below this line the satellites have stellar masses of $M_{\star} \gtrsim 10^7 M_{\odot}$ and are more likely to experience environmental quenching effects. The horizontal dashed line in the upper right-hand panel corresponds to a look-back time of 12.5 Gyr ($z \approx 6$), the end of the epoch of reionization in the simulation.

4.3 Time-scales of environmental quenching

To better understand the connections between ram pressure, infall, and observables such as mass and M_g , we plot the time duration between infall and the closest local ram pressure peak to $t_{\text{gas loss}}$ as a function of satellite M_g colour in Fig. 10. Symbols are the same as Fig. 8 and 9, but we only select satellites that are quenched by the end of the simulation and lose their gas after infall since we want to explore only the effects of environmental quenching.

In general, the left-hand panel of Fig. 10 shows that there is a correlation between t_{delay} time and $t_{\text{infall}} - t_{\text{rp max}}$. Note that we choose $t_{\text{rp max}}$ as the time closest to the quenching time $t_{\text{gas loss}}$ to make sure that we are capturing the most relevant ram pressure stripping event that causes quenching. We shift both t_{delay} and $t_{\text{rp max}}$ by t_{infall} to account for any infall time differences. This correlation shows that ram pressure stripping is one of the main quenching mechanisms, and the scatter indicates that it is not the only mechanisms at play.

The right-hand panel of Fig. 10 shows that faint satellites ($M_g > -12$) reach local ram pressure peak within ≈ 0.5 –1 Gyr after infall and are thus likely quenched by ram pressure stripping of the first pericentric passage shortly after infall. This is also true for a fraction of satellites of intermediate luminosity ($-15 < M_g < -12$). However, a fraction of satellites within this luminosity range experiences peak ram pressure force ~ 2 –7 Gyr after infall, likely after multiple pericentric passages until quenched by a later ram pressure peak. The peak ram pressure force time of the luminous quenched satellites ($M_g < -12$) has the broadest distribution, likely also due to quenching by starvation.

By visually inspecting evolution of the ram pressure force, distance to the host halo centre history, star formation history, and gas fraction history for every satellite, we identify four possible reasons for the scatter of $t_{\text{infall}} - t_{\text{rp max}}$ at a fixed M_g in Fig. 10.

First, there are multiple instances where a satellite loses most of its gas between two peaks in ram pressure force, and it is difficult to conclude which peak is more relevant in quenching the satellite. It is possible that after the first pericentre passage a significant amount of gas is stripped, or it could also be that a significant amount of gas is stripped when the satellite is on its way to the second pericentric passage. Secondly, the estimation of $t_{\text{rp max}}$ itself is uncertain, since some satellites have multiple local peaks that are close to each other around $t_{\text{gas loss}}$. Thirdly, we use a spherically averaged density profile in computing ρ_{CGM} , which is only an approximation to the true local density that the satellite experiences. Fourthly, variations in satellite orbit and impact parameter could also drive a scatter.

Overall, results presented in this section indicate that satellites of mass $M_{\star} \gtrsim 10^7 M_{\odot}$ are quenched mainly after they become satellites by ram pressure stripping. The quenched fraction in this mass range is thus determined by the fraction of satellites that had sufficiently early infall time and had sufficient time to experience significant gas stripping due to ram pressure stripping.

In addition, results presented in this and previous sections indicate that the time-scale of such stripping depends on satellite’s stellar mass and details of its orbit. The smallest mass satellites are quenched shortly after infall, while larger mass satellites exhibit a broad range of quenching time-scales depending on their orbit. This introduces scatter in the quenching time and colour of satellites with similar infall time. Most of the satellites with the largest stellar masses ($M_{\star} \gtrsim 10^8 M_{\odot}$) are not quenched and continue to form stars to $z = 0$. This implies that such massive satellites are resilient against typical ram pressure forces they experience during evolution. At the same time, massive satellites with earliest infall time that could be quenched may not survive to $z = 0$ due to dynamical friction and associated tidal disruption and merging they experience.

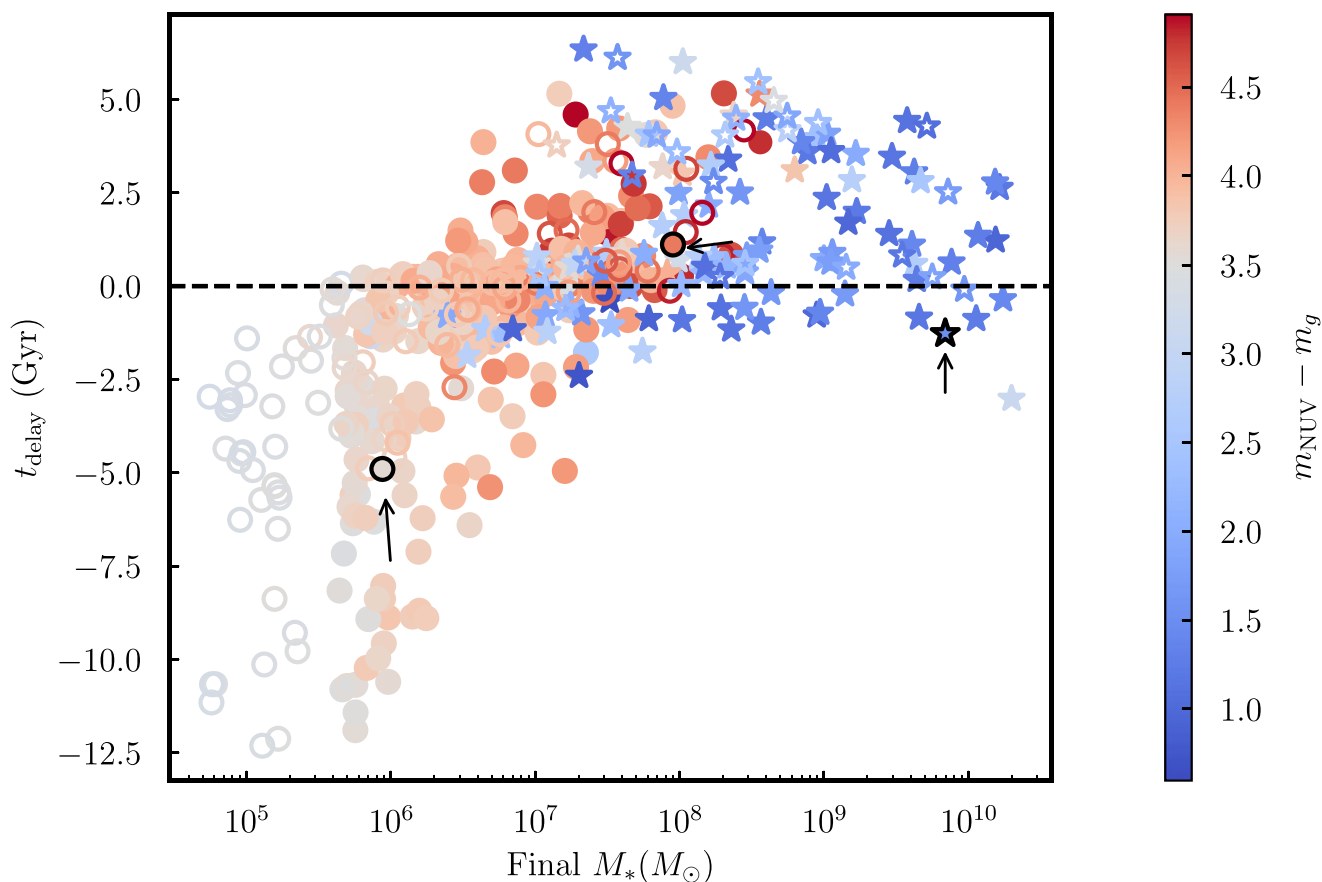


Figure 9. Delay time as a function of final stellar mass. The symbols are the same as in Fig. 8. For quenched satellite galaxies, a negative t_{delay} means they are quenched before infall; here these are primarily satellites with $M_{\star} \lesssim 10^6 M_{\odot}$ in the lower left.

5 DISCUSSION

5.1 Comparison with observations

In recent years, larger and deeper observations have granted us an unprecedented sample of dwarf satellites around MW analogues, important probes of galaxy formation and the nature of dark matter. In particular, Satellites Around Galactic Analogues (SAGA; Geha et al. 2017; Mao et al. 2021) contains classical bright satellites ($M_r < -12.3$ mag) of 100 MW-analogues in the distance range $20 < D < 40$ Mpc. There has been an ongoing tension between SAGA and simulations such as APOSTLE (A Project Of Simulating The Local Environment; Fattahi et al. 2016; Sawala et al. 2016), the DC Justice League simulations (Applebaum et al. 2021), ARTEMIS (Font et al. 2020), and Auriga, where SAGA found significantly more star-forming, low-mass satellites than these simulations (Akins et al. 2021; Karunakaran et al. 2021). Although the large discrepancy between simulations and observations in terms of satellite quenching fraction in the low-mass regime can be potentially mitigated by considering the differences in host mass distributions and observation selection effects (Font et al. 2022), the question of whether simulations can reproduce observations has persisted until the release of the ELVES Survey.

Compared to SAGA, the quenched fraction of satellites in the ELVES sample is more consistent with the results from simulations. Here, we take the ELVES data and look into the colour distribution of satellites to understand the different quenching mechanisms and the time-scales at play. We found the NUV- g colour distributions across

Auriga and ELVES are similar, with a prominent red peak at around $m_{\text{NUV}} - m_g = 3.5$ and another more extended and lower blue peak at around $m_{\text{NUV}} - m_g = 2$. However, the red peak in Auriga is higher and more concentrated to larger values than ELVES, and the blue peak in ELVES is higher and less extended than that in Auriga. We note that we are using the FSPS default MIST isochrones, Chabrier IMF, and MILES spectral library, and that different isochrone models will produce different colours.

Observationally, ELVES classify late- and early-type satellites by visually inspecting the morphology, which is not a direct method for classifying star-formation activity, unlike setting a threshold SFR, which is the criterion of separating star-forming and quenched satellites we used in Auriga. The discrepancy of the two colour distributions might be due to the different classification methods being used.

Finally, there might be sources other than the stars that emit NUV light, which means that the NUV- g colour distribution does not cleanly distinguish the satellite star-formation activity.

Some observational studies also characterized quenching time-scales, which are typically much harder to infer from observations. For example, Fillingham et al. (2019) characterized the infall time for the population of MW satellite galaxies using *Gaia* DR2 proper motion measurements from Fritz et al. (2018). They found that the inferred quenching time-scales for satellites of the MW within the mass range of $10^5 M_{\odot} \lesssim M_{\star} \lesssim 10^8 M_{\odot}$ is consistent with rapid cessation of star formation after infall (Fillingham et al. 2015, 2016, 2018), while satellites with mass $M_{\star} < 10^5 M_{\odot}$ are primarily

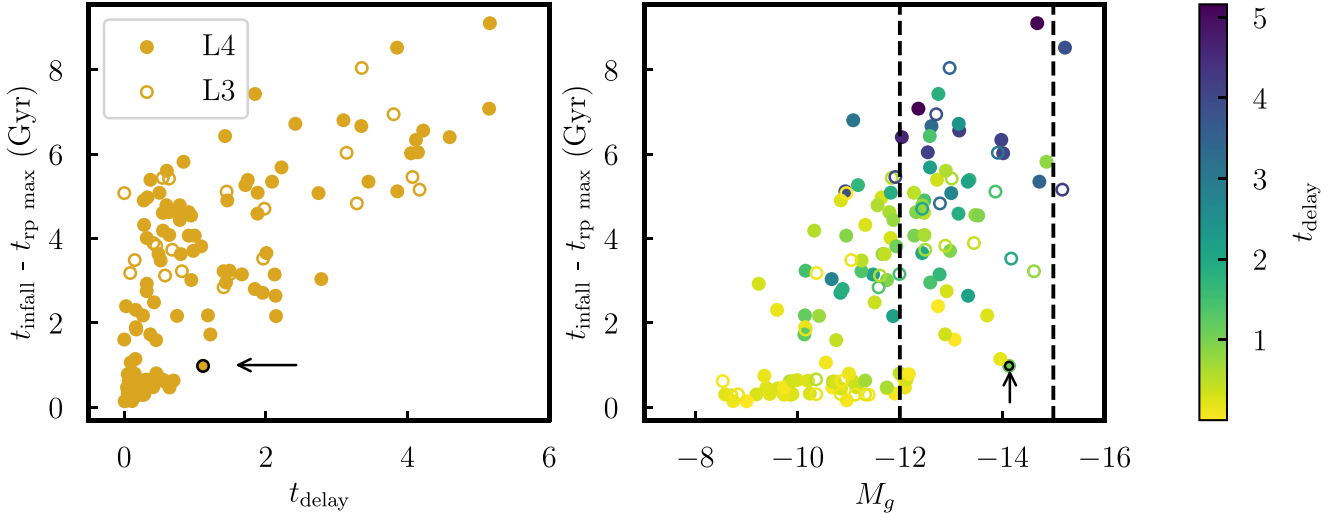


Figure 10. Left-hand panel: Time interval between infall and local ram pressure peak after infall as a function of t_{delay} , for all quenched satellites at $z = 0$ that lose their gas after infall. Halo 2 subhalo 11 in Fig. 5 that loses its gas after infall is indicated by a black arrow. We see a correlation that the higher t_{delay} in general has higher $t_{\text{infall}} - t_{\text{rp max}}$, albeit with some scatter. Right-hand panel: Time interval between infall and local ram pressure peak after infall as a function of the g -band absolute magnitude, M_g , colour coded by t_{delay} , for all quenched satellites at $z = 0$ that lose their gas after infall. The colour bar is set such that the colour divergence starts at $t_{\text{delay}} = 0$, delineating positive and negative t_{delay} . Halo 2 subhalo 11 is indicated by a black arrow. We do not include subhalo 2 and subhalo 28 of halo 1 and because the former is still star-forming at $z = 0$ and the latter is quenched before infall. The open (solid) symbols refer to Level 3 (Level 4) satellites. Lower mass satellites with $M_* \leq 10^6 M_\odot$ generally reach a local ram pressure peak immediately after infall, indicating that ram pressure stripping is their main quenching process. They also have a negative or close to 0 t_{delay} . Some of the intermediate mass satellites, $10^6 M_\odot \leq M_* \leq 10^8 M_\odot$ are also immediately quenched by ram pressure after infall, but a fraction is quenched on much longer time-scales after infall, consistent with a positive t_{delay} . The most massive satellites ($M_* \gtrsim 10^8 M_\odot$) tend to reach the ram pressure peak on much longer time-scales after infall.

quenched by reionization at early cosmic times, in agreement with our results. Figs 8 and 9 show that ultra-faint dwarfs (UFDs) at a critical mass scale of $M_* \sim 10^5 M_\odot$ and have a quenching time-scale τ_{90} close to the end of reionization, and that satellites of mass $10^5 M_\odot \lesssim M_* \lesssim 10^7 M_\odot$ have either a negative or close to 0 delay time.

Moreover, Fig. 3 shows that the Auriga simulations lack blue, low-luminosity satellites that exist in observations such as ELVES. To test if Auriga has these satellites at all, we computed NUV- g colours for all satellites in the high-resolution region (< 1 Mpc from each host). However, we do not find any faint, blue satellites at all in the high-resolution region, suggesting that an issue of the model is at play here. In this faint regime of low mass satellites ($M_g > -12$), our model appears to fail to capture satellite star formation histories. This appears not to be due to a lack of resolution, as L3 and L4 demonstrate the same trends, but due to the model itself.

One possible explanation for this discrepancy is the lack of low-temperature/molecular gas cooling in the stellar feedback and interstellar medium (ISM) model employed in the Auriga simulations. Auriga uses the subgrid ISM model of Springel & Hernquist (2003), which does not directly simulate the dense molecular gas but rather assumes it to be below the resolution of gas cells and treats it as in pressure equilibrium with the hot phase of the ISM. For faint satellites, when the UV radiation disturbs the gas, the effect of molecular gas self-shielding is likely underestimated. These cells therefore heat and stop forming stars more quickly than they should. In low-mass satellites, this effect likely prevents extended, low-level star formation that would make the system bluer, causing the lack we see in Fig. 3. For example, in simulations of a dwarf galaxy heavily influenced by UV heating, Simpson et al. (2013) found that dense molecular gas could continue to self-shield, extending the SFH of an

isolated dwarf system that would otherwise be quenched by external UV heating.

5.2 Comparison with previous theoretical studies

In this section, we compare our results of satellite infall time and colour distribution, satellite quenched fraction, and time-scales to previous theoretical studies. In general, we found reasonably good agreement among different simulations with different underlying physics in terms of quenching time-scales and quenched fraction across the mass range $10^5 M_\odot < M_* < 10^{11} M_\odot$. We explore directly, for the first time, possible connections between satellite's position in the colour-magnitude parameter space and quenching time-scales and mechanisms.

In recent years, theoretical studies have generally agreed upon the different quenching mechanisms operating on different mass scales. Lower mass satellites ($M_* < 10^6 M_\odot$) tend to quench as centrals (Simpson et al. 2018; Fillingham et al. 2019; Akins et al. 2021; Samuel et al. 2022), likely either by reionization at an early cosmic time, internal processes such as stellar feedback, or pre-infall environmental processes. By adding Auriga Level 3 data in our analysis, we probe into the regime of ultra-faint dwarfs ($M_* < 10^5 M_\odot$). In Figs 8 and 9, we show that UFDs have a quenching time-scale τ_{90} close to the end of reionization. For satellites within the mass range $10^5 M_\odot < M_* < 10^6 M_\odot$, we show that they have a negative t_{delay} indicating that they are quenched before infall, in agreement with the scenario that low-mass satellites quench as centrals.

Intermediate-mass satellites ($M_* \sim 10^6 - 10^8 M_\odot$) tend to be quenched by environmental processes after infall, and the quenching time-scale is rapid (Wetzel et al. 2015; Akins et al. 2021; Samuel

et al. 2022), i.e. $t_{\text{delay}} \lesssim 2$ Gyr. A critical stellar mass scale of $10^8 M_{\odot}$ is identified by Akins et al. (2021), where above this value satellites typically are resistant to quenching events and below this threshold satellites are quenched either by non-environmental processes such as reionization and stellar feedback or environmental processes such as ram pressure stripping. Our results in Fig. 9 are consistent with this picture where we also see a transition of negative to positive t_{delay} around stellar mass $10^8 M_{\odot}$.

For massive satellites ($M_{\star} > 10^8 M_{\odot}$), the quenching time-scale is constrained by the gas depletion time (‘starvation’) and is not influenced by rapid environmental quenching effects (Wetzel et al. 2015). Moreover, Joshi et al. (2021) found that in the case of satellites, dwarf systems with the highest satellite mass to host mass ratios have the most extended stellar mass assembly and the smallest τ_{90} , which means that they can better resist environmental effects of their host and retain more gas in their reservoir, confirming our result in Fig. 8 that satellites of higher stellar mass have a lower value of τ_{90} .

In this study, we focused on the intermediate luminosity range $-15 < M_g < -12$, where we see a transition of blue to red satellite galaxies in the CMD of both ELVES and Auriga satellites, and we identified environmental effects to be the dominant quenching mechanism for satellites in this luminosity range. In particular, we looked at the effect of ram pressure stripping in detail. Several other studies also looked at the role of ram pressure stripping on satellite quenching. Buck et al. (2019) followed Simpson et al. (2018) to calculate ram pressure and found that the sharp drop in gas fraction corresponds to the satellites approaching pericentre and thus experiencing an increased amount of ram pressure acting on their gas reservoir, which agrees with our results in Fig. 5. For lower mass satellite the ram pressure spikes up quickly after infall, shortly before their first pericentre and it quickly removes all the gas, whereas for higher mass satellites, they typically can resist the effect of ram pressure and still retain some gas after infall and the first pericentre passage (Buck et al. 2019), confirming our results for satellites of different mass in Fig. 5.

Several studies also identified ram pressure stripping, although not being the only quenching mechanism, is the dominant quenching mechanism for satellites with intermediate stellar mass $10^6 M_{\odot} \lesssim M_{\star} \lesssim 10^8 M_{\odot}$ (Simpson et al. 2018; Buck et al. 2019; Akins et al. 2021), which confirms our result in Fig. 10 that lower mass/faint systems ($M_g > -12$) typically reach a local ram pressure peak < 1 Gyr after infall, and their t_{delay} is close to 0, which indicates that they are quenched mostly by ram pressure shortly after infall. Moreover, we find that intermediate luminosity/mass satellites that are quenched generally have a longer t_{delay} . They are not quenched by ram pressure on the first pericentric passage, but might be quenched by later pericentric passages or starvation, which is indicated by the large scatter in Fig. 10.

Finally, striking commonalities in terms of the quenched fraction in different simulations are also reported by Sales et al. (2022), indicating that this is a basic trend for every simulation no matter the underlying physics.

6 SUMMARY AND CONCLUSIONS

This study is the first comparison between the new ELVES survey and the Auriga simulations. Our main results are summarized below:

(i) We confirm that simulations successfully capture intrinsic satellite galaxy properties such as the luminosity function (Fig. 1), quenched fraction across a wide range of satellite mass (Fig. 2), and the colour–magnitude distribution (Fig. 3) from the ELVES and SAGA surveys. This demonstrates that we can trust simulations

to probe into satellite observables such as colour and magnitude, and more importantly, we can use simulations to explore satellite properties such as infall time and different quenching time-scales that are otherwise hard to obtain in observations.

(ii) We focus on the magnitude range $-15 < M_g < -12$ where ELVES found two distinct populations in terms of their NUV- g colour. These two populations are also present in our colour–magnitude diagram (Fig. 3) where there is a clear transition phase within this magnitude range. We also found two distinct populations in terms of their NUV- g colour in the Auriga simulations (Fig. 4), and we confirmed the results in Simpson et al. (2018) that there are also two distinct populations in terms of infall time in the Auriga simulations (Fig. 6)

(iii) To better understand the origin of this transition phase in terms of satellite colour, we look into different satellite quenching time-scales in the Auriga simulations. We found that low-luminosity satellites ($M_g > -12$) typically quench before infall (negative t_{delay} , Figs 8 and 9), likely by internal processes such as stellar feedback or by reionization. Luminous satellites ($M_g < -15$) are able to retain their gas reservoir even after infall into the host and thus are mostly still star forming. Within the magnitude range $-15 < M_g < -12$, satellites are either star-forming or quenched, and for the quenched ones, they have a positive t_{delay} which indicates that they are quenched by environmental processes after infall. Thus, we confirm that the two distinct populations in the NUV- g colour distribution is caused by environmental quenching after infall.

(iv) We show that ram pressure stripping operates on a fast time-scale ($\lesssim 1$ Gyr) for low-luminosity satellites ($M_g > -12$) upon infall in Fig. 10. For intermediate-luminosity satellites ($-15 < M_g < -12$), few of them are quenched when they reach a local ram pressure peak immediately after infall; they experience a more prolonged quenching history either from later pericentre passages or starvation that gradually strips away all the gas. For luminous satellites, they are able to resist ram pressure and still retain their gas reservoir at the present day.

(v) Lastly, we found that the Auriga simulations lack a population of faint, blue satellites compared to observations such as ELVES. One possible explanation is the underestimation of molecular gas self-shielding in low-mass systems due to the lack of molecular gas cooling in the Auriga ISM model. Future simulations will need to model the dense molecular gas more carefully to better reproduce observations in terms of the colour–magnitude distribution.

ACKNOWLEDGEMENTS

The authors thank the anonymous referee for constructive suggestions on the manuscript. We acknowledge support from the University of Chicago’s Research Computing Center and the Enrico Fermi Institute. The authors would like to thank Scott Carlsten, Jenny Greene, and the ELVES team for helpful discussion of the comparison between ELVES sample and the Auriga simulations. We also thank Phil Mansfield for comments on the figures, and Yao-Yuan Mao for kindly sharing the SAGA data. This work was supported by the Enrico Fermi Institute at the University of Chicago, by the National Science Foundation grants AST-1714658 and AST-1911111 and NASA ATP grant 80NSSC20K0512. FAG acknowledges support from ANID FONDECYT Regular 1211370 and by the ANID BASAL project FB210003. FAG acknowledges funding from the Max Planck Society through a ‘Partner Group’ grant. Analyses in this paper were greatly aided by the following free software packages: NUMPY (van der Walt, Colbert & Varoquaux 2011), SCIPY (Jones, Oliphant & Peterson 2001), ASTROPY (Astropy

Collaboration 2018), and MATPLOTLIB (Hunter 2007). This research has also made extensive use of Astrophysics Data Service (ADS) and arXiv preprint repository.

DATA AVAILABILITY

The data underlying this article will be shared on reasonable request to the authors.

REFERENCES

- Agertz O., Kravtsov A. V., Leitner S. N., Gnedin N. Y., 2013, *ApJ*, 770, 25
- Akins H. B., Christensen C. R., Brooks A. M., Munshi F., Applebaum E., Engelhardt A., Chamberland L., 2021, *ApJ*, 909, 139
- Applebaum E., Brooks A. M., Christensen C. R., Munshi F., Quinn T. R., Shen S., Tremmel M., 2021, *ApJ*, 906, 96
- Astropy Collaboration 2018, *AJ*, 156, 123
- Bahé Y. M., McCarthy I. G., 2015, *MNRAS*, 447, 969
- Baldry I. K., Glazebrook K., Brinkmann J., Ivezić Ž., Lupton R. H., Nichol R. C., Szalay A. S., 2004, *ApJ*, 600, 681
- Behroozi P. S., Wechsler R. H., Lu Y., Hahn O., Busha M. T., Klypin A., Primack J. R., 2014, *ApJ*, 787, 156
- Bell E. F. et al., 2004, *ApJ*, 608, 752
- Benítez-Llambay A., Navarro J. F., Abadi M. G., Gottlöber S., Yepes G., Hoffman Y., Steinmetz M., 2013, *ApJ*, 763, L41
- Bose S., Deason A. J., Frenk C. S., 2018, *ApJ*, 863, 123
- Brown T. M. et al., 2014, *ApJ*, 796, 91
- Bruzual G., Charlot S., 2003, *MNRAS*, 344, 1000
- Buck T., Macciò A. V., Dutton A. A., Obreja A., Frings J., 2019, *MNRAS*, 483, 1314
- Carlsten S. G., Greene J. E., Beaton R. L., Danieli S., Greco J. P., 2022, *ApJ*, 933, 47
- Chabrier G., 2003, *PASP*, 115, 763
- Choi J., Dotter A., Conroy C., Cantiello M., Paxton B., Johnson B. D., 2016, *ApJ*, 823, 102
- Conroy C., Gunn J. E., 2010, *ApJ*, 712, 833
- Conroy C., Gunn J. E., White M., 2009, *ApJ*, 699, 486
- Davies L. J. M. et al., 2016, *MNRAS*, 455, 4013
- Davis M., Efstathiou G., Frenk C. S., White S. D. M., 1985, *ApJ*, 292, 371
- De Lucia G., Blaizot J., 2007, *MNRAS*, 375, 2
- Dekel A., Silk J., 1986, *ApJ*, 303, 39
- Digby R. et al., 2019, *MNRAS*, 485, 5423
- Dotter A., 2016, *ApJS*, 222, 8
- Emerick A., Mac Low M.-M., Grcevich J., Gatto A., 2016, *ApJ*, 826, 148
- Falcón-Barroso J., Sánchez-Blázquez P., Vazdekis A., Ricciardelli E., Cardiel N., Cenarro A. J., Gorgas J., Peletier R. F., 2011, *A&A*, 532, A95
- Fattahi A. et al., 2016, *MNRAS*, 457, 844
- Fillingham S. P. et al., 2019, preprint ([arXiv:1906.04180](https://arxiv.org/abs/1906.04180))
- Fillingham S. P., Cooper M. C., Boylan-Kolchin M., Bullock J. S., Garrison-Kimmel S., Wheeler C., 2018, *MNRAS*, 477, 4491
- Fillingham S. P., Cooper M. C., Pace A. B., Boylan-Kolchin M., Bullock J. S., Garrison-Kimmel S., Wheeler C., 2016, *MNRAS*, 463, 1916
- Fillingham S. P., Cooper M. C., Wheeler C., Garrison-Kimmel S., Boylan-Kolchin M., Bullock J. S., 2015, *MNRAS*, 454, 2039
- Font A. S. et al., 2020, *MNRAS*, 498, 1765
- Font A. S., McCarthy I. G., Belokurov V., Brown S. T., Stafford S. G., 2022, *MNRAS*, 511, 1544
- Fraternali F., Tolstoy E., Irwin M. J., Cole A. A., 2009, *A&A*, 499, 121
- Fritz T. K., Battaglia G., Pawlowski M. S., Kallivayalil N., van der Marel R., Sohn S. T., Brook C., Besla G., 2018, *A&A*, 619, A103
- Garrison-Kimmel S. et al., 2019, *MNRAS*, 489, 4574
- Geha M. et al., 2017, *ApJ*, 847, 4
- Geha M., Blanton M. R., Yan R., Tinker J. L., 2012, *ApJ*, 757, 85
- Gnedin N. Y., 2000, *ApJ*, 535, 530
- Grand R. J. J. et al., 2017, *MNRAS*, 467, 179
- Grand R. J. J. et al., 2021, *MNRAS*, 507, 4953
- Grcevich J., Putman M. E., 2009, *ApJ*, 696, 385
- Gunn J. E., Gott J. Richard I., 1972, *ApJ*, 176, 1
- Hausammann L., Revaz Y., Jablonka P., 2019, *A&A*, 624, A11
- Huang S., Haynes M., Giovanelli R., Brinchmann J., Stierwalt S., Neff S., 2012, American Astronomical Society Meeting Abstracts, Vol. 219, 441.23
- Hunter J. D., 2007, *Comput. Sci. Eng.*, 9, 90
- Jones E., Oliphant T., Peterson P., 2001, SciPy: Open Source Scientific Tools for Python. Available at: <http://www.scipy.org>
- Joshi G. D., Pillepich A., Nelson D., Zinger E., Marinacci F., Springel V., Vogelsberger M., Hernquist L., 2021, *MNRAS*, 508, 1652
- Karachentsev I. D., Makarova L. N., Makarov D. I., Tully R. B., Rizzi L., 2015, *MNRAS*, 447, L85
- Karunakaran A. et al., 2021, *ApJ*, 916, L19
- Karunakaran A., Sand D. J., Jones M. G., Spekkens K., Bennet P., Crnojević D., Mutlu-Pakdil B., Zaritsky D., 2022, preprint ([arXiv:2210.03748](https://arxiv.org/abs/2210.03748))
- Kazantzidis S., Mayer L., Callegari S., Doti M., Moustakas L. A., 2017, *ApJ*, 836, L13
- Knuth K. H., 2006, preprint (physics/0605197)
- Kravtsov A., Manwadkar V., 2022, *MNRAS*, 514, 2667
- Lewis G. F., Ibata R. A., Chapman S. C., McConnachie A., Irwin M. J., Tolstoy E., Tanvir N. R., 2007, *MNRAS*, 375, 1364
- Lin D. N. C., Faber S. M., 1983, *ApJ*, 266, L21
- Makarov D., Makarova L., Sharina M., Uklein R., Tikhonov A., Guhathakurta P., Kirby E., Terekhova N., 2012, *MNRAS*, 425, 709
- Mao Y.-Y., Geha M., Wechsler R. H., Weiner B., Tollerud E. J., Nadler E. O., Kallivayalil N., 2021, *ApJ*, 907, 85
- Mateo M. L., 1998, *ARA&A*, 36, 435
- Mayer L., Governato F., Colpi M., Moore B., Quinn T., Wadsley J., Stadel J., Lake G., 2001, *ApJ*, 559, 754
- Mayer L., Mastrogiuseppe C., Wadsley J., Stadel J., Moore B., 2006, *MNRAS*, 369, 1021
- McConnachie A. W., 2012, *AJ*, 144, 4
- McGee S. L., Bower R. G., Balogh M. L., 2014, *MNRAS*, 442, L105
- Menci N., Fontana A., Giallongo E., Salimbeni S., 2005, *ApJ*, 632, 49
- Murakami I., Babul A., 1999, *MNRAS*, 309, 161
- Pakmor R., Springel V., Bauer A., Mocz P., Muñoz D. J., Ohlmann S. T., Schaal K., Zhu C., 2016, *MNRAS*, 455, 1134
- Pearson S. et al., 2016, *MNRAS*, 459, 1827
- Pearson S. et al., 2018, *MNRAS*, 480, 3069
- Phillips J. I., Wheeler C., Cooper M. C., Boylan-Kolchin M., Bullock J. S., Tollerud E., 2015, *MNRAS*, 447, 698
- Putman M. E., Zheng Y., Price-Whelan A. M., Grcevich J., Johnson A. C., Tollerud E., Peek J. E. G., 2021, *ApJ*, 913, 53
- Rey M. P., Pontzen A., Agertz O., Orkney M. D. A., Read J. I., Rosdahl J., 2020, *MNRAS*, 497, 1508
- Rey M. P., Pontzen A., Agertz O., Orkney M. D. A., Read J. I., Saintonge A., Kim S. Y., Das P., 2022, *MNRAS*, 511, 5672
- Richings J. et al., 2020, *MNRAS*, 492, 5780
- Rodriguez Wimberly M. K., Cooper M. C., Fillingham S. P., Boylan-Kolchin M., Bullock J. S., Garrison-Kimmel S., 2019, *MNRAS*, 483, 4031
- Sales L. V., Wetzel A., Fattahi A., 2022, *Nat. Astron.*, 6, 897–910
- Samuel J., Wetzel A., Santistevan I., Tollerud E., Moreno J., Boylan-Kolchin M., Bailin J., Pardasani B., 2022, *MNRAS*, 514, 5276
- Sawala T. et al., 2016, *MNRAS*, 457, 1931
- Simpson C. M., Bryan G. L., Johnston K. V., Smith B. D., Mac Low M.-M., Sharma S., Tumlinson J., 2013, *MNRAS*, 432, 1989
- Simpson C. M., Grand R. J. J., Gómez F. A., Marinacci F., Pakmor R., Springel V., Campbell D. J. R., Frenk C. S., 2018, *MNRAS*, 478, 548
- Slater C. T., Bell E. F., 2014, *ApJ*, 792, 141
- Spekkens K., Urbancic N., Mason B. S., Willman B., Aguirre J. E., 2014, *ApJ*, 795, L5
- Springel V. et al., 2005, *Nature*, 435, 629
- Springel V., 2010, *MNRAS*, 401, 791
- Springel V., Hernquist L., 2003, *MNRAS*, 339, 289
- Springel V., White S. D. M., Tormen G., Kauffmann G., 2001, *MNRAS*, 328, 726
- Strateva I. et al., 2001, *AJ*, 122, 1861
- Thoul A. A., Weinberg D. H., 1996, *ApJ*, 465, 608
- Tollerud E. J., Peek J. E. G., 2018, *ApJ*, 857, 45
- Tonnesen S., Bryan G. L., 2009, *ApJ*, 694, 789

- Trussler J., Maiolino R., Maraston C., Peng Y., Thomas D., Goddard D., Lian J., 2020, *MNRAS*, 491, 5406
- van den Bosch F. C., Aquino D., Yang X., Mo H. J., Pasquali A., McIntosh D. H., Weinmann S. M., Kang X., 2008, *MNRAS*, 387, 79
- van der Walt S., Colbert S. C., Varoquaux G., 2011, *Comput. Sci. Eng.*, 13, 22
- Vazdekis A., Sánchez-Blázquez P., Falcón-Barroso J., Cenarro A. J., Beasley M. A., Cardiel N., Gorgas J., Peletier R. F., 2010, *MNRAS*, 404, 1639
- Vogelsberger M., Genel S., Sijacki D., Torrey P., Springel V., Hernquist L., 2013, *MNRAS*, 436, 3031
- Weisz D. R., Dolphin A. E., Skillman E. D., Holtzman J., Gilbert K. M., Dalcanton J. J., Williams B. F., 2014, *ApJ*, 789, 148
- Weisz D. R., Dolphin A. E., Skillman E. D., Holtzman J., Gilbert K. M., Dalcanton J. J., Williams B. F., 2015, *ApJ*, 804, 136
- Wetzel A. R., Tinker J. L., Conroy C., van den Bosch F. C., 2013, *MNRAS*, 432, 336
- Wetzel A. R., Tollerud E. J., Weisz D. R., 2015, *ApJ*, 808, L27
- Wheeler C., Phillips J. I., Cooper M. C., Boylan-Kolchin M., Bullock J. S., 2014, *MNRAS*, 442, 1396
- White S. D. M., Frenk C. S., 1991, *ApJ*, 379, 52

This paper has been typeset from a $\text{\TeX}/\text{\LaTeX}$ file prepared by the author.